Pyramid-Shaped Wurtzite CdSe Nanocrystals with Inverted Polarity

Sandeep Ghosh,[†] Roberto Gaspari,[‡] Giovanni Bertoni,[†,§] Maria Chiara Spadaro,[⊥] Mirko Prato,[†] Stuart Turner,[∥] Andrea Cavalli,[#,‡,▽] Liberato Manna,[*,†] and Rosaria Brescia[*,†]

[†]Department of Nanochemistry, Istituto Italiano di Tecnologia (IIT), via Morego 30, I-16163 Genova, Italy, [‡]CONCEPT Lab, Istituto Italiano di Tecnologia (IIT), via Morego 30, I-16163 Genova, Italy, [§]IMEM-CNR, Parco Area delle Scienze 37/A, I-43124 Parma, Italy, [⊥]CNR-NANO, Centro di Ricerca S3 & Dipartimento di Fisica, Informatica e Matematica (FIM), Università di Modena e Reggio Emilia, via G. Campi 213/A, I-41125 Modena, Italy, [∥]EMAT, University of Antwerp, Groenenborgerlaan 171, B-2020 Antwerp, Belgium, [#]CompuNet, Istituto Italiano di Tecnologia (IIT), via Morego 30, I-16163 Genova, Italy, and [▽]Department of Pharmacy and Biotechnology, University of Bologna, via Belmeloro 6, I-40126 Bologna, Italy

ABSTRACT We report on pyramid-shaped wurtzite cadmium selenide (CdSe) nanocrystals (NCs), synthesized by hot injection in the presence of chloride ions as shape-directing agents, exhibiting reversed crystal polarity compared to former reports. Advanced transmission electron microscopy (TEM) techniques (image-corrected high-resolution TEM with exit wave reconstruction and probe-corrected high-angle annular dark field-scanning TEM) unequivocally indicate that the triangular base of the pyramids is the polar (000$\bar{1}$) facet and their apex points toward the [0001] direction. Density functional theory calculations, based on a simple model of binding of Cl^- ions to surface Cd atoms, support the experimentally evident higher thermodynamic stability of the (000$\bar{1}$) facet over the (0001) one conferred by Cl^- ions. The relative stability of the two polar facets of wurtzite CdSe is reversed compared to previous experimental and computational studies on Cd chalcogenide NCs, in which no Cl-based chemicals were deliberately used in the synthesis or no Cl^- ions were considered in the binding models. Self-assembly of these pyramids in a peculiar clover-like geometry, triggered by the addition of oleic acid, suggests that the basal (polar) facet has a density and perhaps type of ligands significantly different from the other three facets, since the pyramids interact with each other exclusively *via* their lateral facets. A superstructure, however with no long-range order, is observed for clovers with their (000$\bar{1}$) facets roughly facing each other. The CdSe pyramids were also exploited as seeds for CdS pods growth, and the peculiar shape of the derived branched nanostructures clearly arises from the inverted polarity of the seeds.

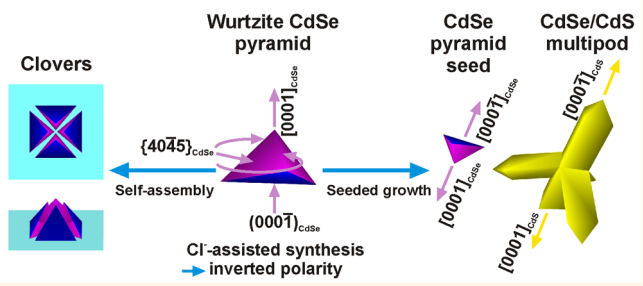

KEYWORDS: colloidal synthesis · CdSe nanocrystals · chloride assisted · crystal polarity · self-assembly

The importance of colloidal synthesis of semiconductor nanocrystals (NCs) can be envisaged from their use in a broad range of fields like photovoltaics,[1] optoelectronic devices,[2] biomarking[3,4] and digital displays.[5] It is therefore of paramount importance that both efficient synthesis protocols to obtain high quality NCs of well-defined shapes and sizes and the mechanisms leading to the same are carefully investigated.[6] Hot-injection is a versatile technique in the colloidal synthesis paradigm, as it provides a high degree of control over the NC size and shape distribution and over the nature of the stabilizing agent (ligand shell), as exemplified in case of the various transition metal chalcogenides[7−10] and pnictides.[11−13] In this regard, impurities play a major role in colloidal synthesis as they,[14] whether introduced accidentally or already present in the chemicals used, can lead to reproducibility issues, as illustrated for the role of tri-*n*-octylphosphine oxide (TOPO) in the growth of cadmium selenide NCs[15−17] and that of *in situ* formed acetate ions for lead selenide NCs.[18,19] Halide ions are a source of impurities which has come under intense scrutiny very recently, as can be envisaged from the numerous literature reports describing their influence on the growth of NCs of various materials such as lead chalcogenides,[20−23] nickel sulfide,[24] copper sulfide,[24] and noble metals.[25−27] Halide ions were found to exhibit a strong influence on the growth and transformation of cadmium chalcogenide NCs as well.[28−33] For instance, in a previous report from our group, we described the shape evolution of heterostructured octapod-shaped CdSe(core)/CdS(pods) NCs, a morphology not easily

* Address correspondence to liberato.manna@iit.it, rosaria.brescia@iit.it.

Received for review June 15, 2015 and accepted July 23, 2015.

Published online July 23, 2015
10.1021/acsnano.5b03636

accessible, due to the incorporation of chloride ions in the synthesis environment.[28] This unique structure could be obtained due to the formation of strong complexes of Cd with Cl leading to the reduced availability of Cd in solution, thus furnishing an enhanced ability to play with nucleation and growth kinetics. Similarly, the role of Cl^- ions as morphological transformers[29] and active anisotropic etchants of preformed cadmium chalcogenide NCs, giving rise to altered shapes,[30] has also been documented. Also, Palencia *et al.* have demonstrated the transformation of initial rod-like CdSe NCs into pyramids under the influence of Cl^- anions, released through a reaction between tri-*n*-octylphosphine (TOP) and 1,2-dichloroethane (DCE).[31,34] The authors concluded that the chlorinated species formed *in situ*, by the reaction between TOP (or TOP@Se) and DCE, were actually responsible for the shape transformation.

Here we describe the synthesis of nearly monodisperse pyramidal wurtzite CdSe nanoparticles (NPYs), such morphology being attainable due to the presence of Cl^- ions in the reaction mixture and initially delivered as cadmium chloride ($CdCl_2$). Selected-area electron diffraction (SAED) patterns and high-resolution transmission electron microscopy (HRTEM) analyses reveal that the dominant phase is wurtzite CdSe, albeit several NPYs exhibit zinc-blende CdSe stacking faults as well. HRTEM focal series were acquired on suitably oriented NPYs and the complex wave function of the electrons after they have passed through the sample, *i.e.*, the exit wave (EW), was retrieved. The EW phase enables the unequivocal identification of the two atomic columns in the Cd−Se dumbbells, thanks to their different atomic numbers. These results are further corroborated by Z-contrast imaging of NPYs by atomic resolution high-angle annular dark field-scanning TEM (HAADF-STEM) imaging. Two types of crystal facets, characterized by different polarity, constitute the NPYs: the equilateral basal facet of the NPYs conforms to the polar $(000\bar{1})$ facet (Figure 1a), while the three (equivalent) lateral facets correspond to $\{40\bar{4}5\}$ nonpolar facets. In all the NPYs analyzed by C_s-corrected HRTEM/HAADF-STEM, the apex points toward the [0001] direction. The absence of a (0001) flat facet indicates its instability under the present growth conditions.

The relative stability of the NPY polar facets markedly differs from previously reported cases, *i.e.*, for cadmium chalcogenide rod-shaped NCs in the wurtzite phase, showing flat ends corresponding to (0001) facets and sharp tips growing toward the $[000\bar{1}]$ direction.[35] Density functional theory (DFT) calculations were performed on possible binding configurations of Cl atoms on (0001) and $(000\bar{1})$ facets. While on the $(000\bar{1})$ facets, Cl^- ions bridging two surface Cd atoms can nicely mimic the presence of Se atoms with minimal bond distortion and with satisfaction of electron counting rules, this is not possible for the

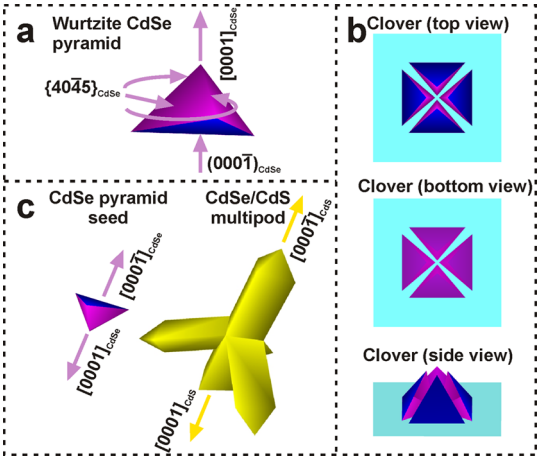

Figure 1. (a) Sketch of a wurtzite CdSe pyramid (NPY); (b) different views of a model of a clover-shaped assembly formed by NPYs with the respective lateral facets (magenta) roughly parallel to each other. In the top view the noninteracting $(000\bar{1})$ facets (in blue) are visible; (c) sketch of a branched nanostructure prepared by seeded growth of wurtzite CdS pods onto a CdSe NPY.

(0001) facet without serious bond distortion. In addition, surface binding of Cl leaves enough room for other molecules to bind and electronically deprives the remaining surface Cd dangling bonds, a situation that would favor the further binding of such Cd atoms to the alkylphosphonic acids present in the growth solution. Overall, it therefore appears that Cl^- ions in the reaction environment bestow higher thermodynamic stability to the $(000\bar{1})$ basal facet.

At our current level of understanding (both experimental and computational) we have no direct proof of differences, both in terms of types of ligands and degree of surface passivation, between the basal and the lateral facets of the NPYs. On the other hand, an indication in this regard comes from self-assembly of the NPYs induced by the addition of oleic acid (OA): a large fraction of NPYs self-organize into "clover-like" tetrameric units (Figure 1b) formed by parallel alignment of their lateral facets, while the basal $(000\bar{1})$ facets are only mildly involved in a short-range superstructure. The acquired higher "stickiness" of the lateral facets, in the presence of OA, suggests interdigitation of the surface ligand with OA molecules, probably present as dimers, and acting as the "glue" bridging two NPYs side to side. For the basal facets, either such interdigitation is less efficient because of the different nature or density of passivation, or they possess residual charge that prevents attractive interactions. Higher order of assembly (larger oligomers or long-range organization) was not observed, and the assembly could not be triggered by other types of molecules (except for aliphatic carboxylic acids such as nonanoic acid).

Finally, the reversed polarity of the NPYs manifests upon their use as seeds in the synthesis of branched nanostructures. These structures are analyzed here

since NCs with branched morphologies are promising for the fabrication of active materials in photovoltaic devices[36] or as local stress sensors with bright luminescence readout,[37] among other fields. Hence, factors pertaining to the growth of such structures are worth being investigated. In this case, wurtzite CdS pods were grown on top of the NPYs, under conditions favoring a higher stability for the (000$\bar{1}$) facets of wurtzite CdS. The resulting rocket-shaped NCs (Figure 1c), analyzed by HAADF-STEM electron tomography, evidences a major pod (the rocket body), presumably evolving from the (000$\bar{1}$) NPY base and exhibiting a sharp tip, and three smaller pods (the rocket wings) nucleated on the lateral facets, all with sharp tips. A much shorter pod, exhibiting a flat end, evolves instead from the NPY apex.

RESULTS AND DISCUSSION

In line with our previous work,[28] $CdCl_2$ was employed here as a Cl^- source for the growth of CdSe NPYs. These NCs were synthesized following the classical hot-injection method wherein a selenium source (Se:TOP) was rapidly injected into a hot mixture of cadmium oxide (CdO), $CdCl_2$, hexylphosphonic acid (HPA) and octadecylphosphonic acid (ODPA) prepared in TOPO as the solvent. Additional details of the synthesis protocol are reported in the Methods section. The growth of the NCs was monitored over time: the pyramidal shape of the particles was evident already after 1 min from the injection, and preserved at least for 5 min (see Figure S1). Aliquots taken at later stages, *e.g.*, after 15, 30, and 60 min from the injection, exhibited signs of ripening, with smoothing of the pyramid corners taking place already after 15 min. Taking into account this shape evolution, the NPYs discussed henceforth were grown only for 5 min. The NPYs were then washed with a toluene-methanol mixture and subjected to size selection using OA as the flocculant (the use of OA to assemble the NCs, once they were purified, will be discussed later). After the first size-selection step (*i.e.*, flocculating with OA, washing with methanol and redispersing in toluene), the NCs appeared rather monodisperse, most of them exhibiting an equilateral triangular projection in bright-field TEM (BFTEM) images (Figure 2a), with an average edge length of 20.3(±0.9) nm. In some areas NCs with an isosceles triangular projection, with an average minor edge length of 16(±2) nm, were found (white circles in Figure 2b), besides the predominant NCs exhibiting an equilateral triangular projection (yellow circles in Figure 2b).

Elemental maps (Figure S2) demonstrate homogeneous distribution of Cd and Se over the NCs, with a Cd/Se atomic ratio of 1.0, viewed along both projections. This result enables the direct interpretation of the contrast in the overview HAADF-STEM images (Figure 2b) as a thickness contrast. Volume reconstruction of these NCs

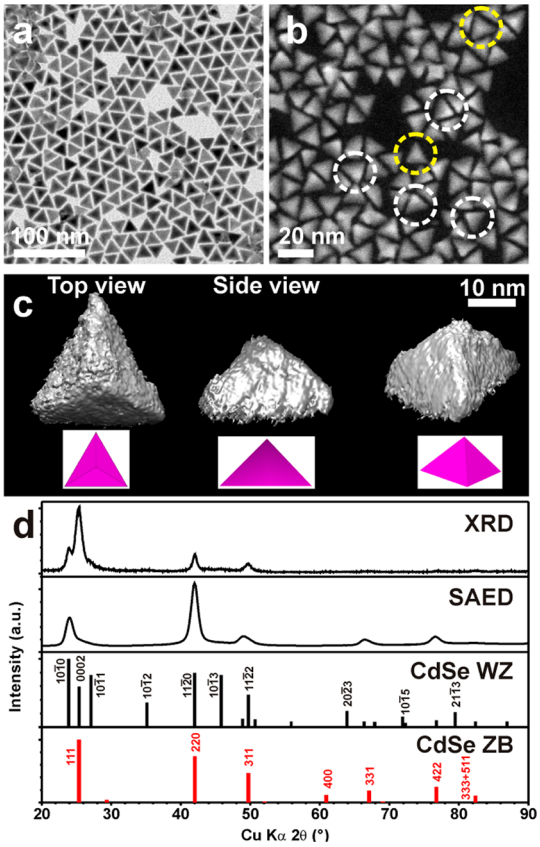

Figure 2. (a) Overview BFTEM image of a group of CdSe NPYs. (b) HAADF-STEM image of a group of NPYs: the thickness-contrast in the two observed projections (yellow circles: equilateral triangle, white circles: isosceles triangle) allows to appreciate the pyramidal shape of the NCs. (c) Isosurface view of reconstructed volume (*via* HAADF-STEM tomography) of a CdSe NPY, viewed along different orientations. (d) XRD pattern and azimuthally integrated SAED pattern for the NCs, compared to database powder XRD patterns for wurtzite (WZ, ICSD #415785) and zinc-blende (ZB, ICSD #41528) CdSe. The most intense peaks in the reference patterns are indexed.

via HAADF-STEM electron tomography also confirms their pyramidal shape corresponding to a slightly flattened tetrahedron (Figure 2c). The combination of X-ray diffraction (XRD) and azimuthally integrated SAED patterns collected from the NPYs (Figure 2d), respectively probing reciprocal lattice vectors perpendicular (XRD) and roughly parallel (SAED) to the support surface, identify the predominance of the wurtzite CdSe phase. The high intensity of Bragg peaks due to the (10$\bar{1}$0) and (11$\bar{2}$0) planes of wurtzite CdSe in the SAED patterns, together with the high intensity of the peak from (0002) planes in the XRD pattern, indicate a strong preferential orientation of the NCs, with the ⟨0001⟩ direction perpendicular to the support surface for most NCs. The optical absorption spectrum of the NPYs is reported in the SI (Figure S3). As a note, the NPYs exhibited no appreciable photoluminescence, probably as a consequence of the types of passivating molecules present on their surface.

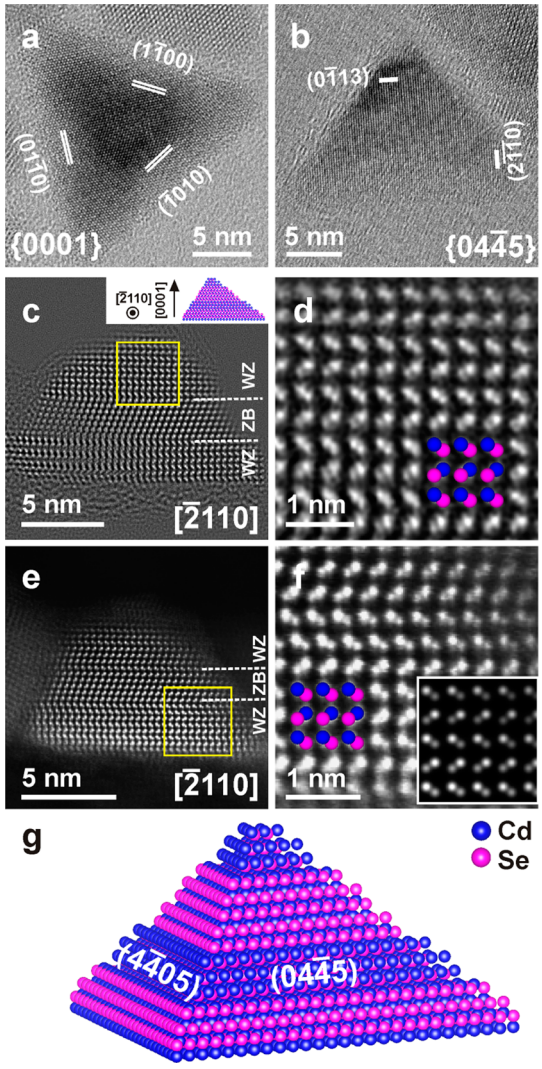

Figure 3. Study of faceting and polarity of the CdSe NPYs. (a,b) HRTEM images of NPYs viewed with (a) the equilateral triangle base and (b) one of the isosceles triangle side facets lying on the carbon support film. (c) HRTEM image of a NPY with the base sticking to the edge of a hole in the carbon film and oriented along [$\bar{2}$110], acquired with $C_s = -30\ \mu$m and −8 nm focus. (d) EW phase obtained from a region close to the NPY tip in (c). (e) Low-pass filtered HAADF image acquired for NPY in analogous orientation as in (c), with magnified area in (f) and compared to simulated image (inset in (f)). (g) Atomic model of a NPY based on the results of C_s-corrected HRTEM and HAADF analyses.

HRTEM analyses of individual particles confirm the ⟨0001⟩-orientation of the NPY apex, with NPYs viewed parallel to the base (Figure 3a). In order to understand the NC polarity, *i.e.*, the orientation of the NPY apex, HRTEM images of the NCs sticking to the holey carbon film walls were acquired along the [$\bar{2}$110] direction (Figure 3c). Along this crystallographic direction, the Cd−Se dumbbells can clearly be resolved, as the Cd and Se atomic columns are about 1.5 Å apart. For this orientation, focal series were acquired in negative spherical aberration conditions, allowing for direct atomic column imaging to some extent.[38] However, the contrast in HRTEM images strongly depends on the thickness of the sample, after the focus in the image is chosen. This makes the identification of the atomic columns (and consequently of the polarity) not straightforward. The pyramidal shape is indeed an example of prominent thickness variation across an image projection from HRTEM. To unequivocally assign the polarity of the exit-wave (EW) reconstruction from a focal series of HRTEM images was performed.[35] The EW is the (complex) wave function at the exit plane of the specimen, after the microscope transfer function (due to the aberrations) has been removed by iterative back-projection. In particular, the EW phase (being proportional to the projected potential) gives a direct visualization of the atomic columns according to their atomic number, *Z*. Cd atoms in the dumbbells, brighter than Se atoms in the phase image due to higher *Z*, point toward the NPY apex (Figure 3d). As a further confirmation, C_s-corrected HAADF images were acquired for NPYs along the same crystallographic orientation (Figure 3e,f), which exhibit brighter columns toward the NPY apex. Note that HAADF has a dominantly incoherent contrast roughly proportional to Z^2. However, given the complex shape of the CdSe NPYs, and in particular their rapidly varying thickness in the chosen projection, experimental HAADF images were compared with simulated ones (inset in Figure 3f). The results confirm the outcome of the EW phase reconstruction from HRTEM images, proving that the latter method leads to correct results also in case of large thickness variation in the crystal. By combining the HRTEM- and HAADF-based polarity information with HRTEM images of NPYs lying with one of the lateral facets on the support film (Figure 3b), it is possible to identify the NPY equilateral triangular base as a (000$\bar{1}$) facet and the three lateral facets as {40$\bar{4}$5} facets (Figure 3g). This crystallographic assessment of the NPY faceting is also in agreement with the electron tomography reconstruction of single NPYs (Figure 2c), showing ∼30° angles between the NPY lateral facets and its base. However, zinc-blende stacking faults are found in HRTEM and HAADF images for several NPYs (Figure 3(c,e)), inducing slight distortions from ideal faceting of single-crystal wurtzite CdSe NCs. The variation of the relative stability of the wurtzite and zinc-blende phases in the presence of Cl^- ions, through insertion of stacking faults in the structure, was already reported by Saruyama *et al.* for CdS, together with shape modification ascribed to Ostwald ripening.[29] Despite the faulty structure, however, the polarity of the NPYs remains the same throughout the NPYs.

The unequivocally demonstrated polarity of the CdSe NPYs is reversed compared to the one reported by Hungria *et al.* for similar NCs synthesized in Cl-containing environments, where the formation of the NPY apex toward the [000$\bar{1}$] direction was deduced from TEM tomography experiments.[39] However, the pyramidal NCs analyzed by Hungria *et al.* are significantly

different from the present ones, as they result from a ripening process taking place over hours, while our NCs exhibited a pyramidal shape already during the early stages of the synthesis (see Figure S1 in the SI). Moreover, our group demonstrated that for wurtzite CdSe/CdS rod-in-rod NCs synthesized in non-Cl-containing environments a flat end was formed toward the [0001] direction and a tip toward the [000$\bar{1}$] one.[35] That morphology was explained based on the higher stability of the (0001) facet in the synthesis environment compared to the Cd-terminated (000$\bar{1}$) facet, due to the many dangling bonds present (three per Cd atom), the latter one being replaced during growth by more stable (and less polar) facets.

These results indicate that the addition of Cl^- ions in the reaction environment reverses the relative stability of the (0001) and (000$\bar{1}$) facets, although they give us no additional clue concerning the type of ligand atoms/molecules on the surface of the NCs, and on whether there is a substantial difference in passivation between the basal and the lateral facets. Ligand exchange experiments, monitored using nuclear magnetic resonance spectroscopy (NMR) and X-ray photoelectron spectroscopy (XPS), described in detail in the SI (section S5), point toward the fact that Cl^- ions make up for a part of the ligand shell, together with alkylphosphonic acids. It is also worthy of note that the phosphorus 2p signal for the NPYs could be deconvoluted into two separate signals, as shown in Figure S6 of the SI, signifying the presence of both phosphonic acid anhydrides and deprotonated phosphonate species, in agreement with previous studies.[40,41]

To get more insights into the involvement of Cl^- ions on the surface of the NCs, we carried out DFT calculations on a simplified model based on bulk CdSe surfaces passivated by Cl atoms only. Since Cl atoms can accept one electron to become Cl^- ions, and Cd atoms can donate two electrons becoming Cd^{2+} ions, we considered complexation only with the Cd-terminated surfaces. Bare Cd terminated surfaces exhibit one dangling bond per Cd atom, for the CdSe(0001) case, and three dangling bond per Cd atom, for the CdSe(000$\bar{1}$) case, respectively. Details of the calculations are reported in the Methods section and in the SI (section S6).

The main criterion in finding stable binding configurations in these types of calculations is the fulfillment of the so-called *electron counting rules*, which essentially means that there can be transfer of electrons from surface cations to surface anions as well as from surface atoms to adsorbates (Cl atoms in this case) so that all atoms involved have their outer shell completed. In some cases, to fulfill this, some surface atoms need to be removed, and a proper choice on the dimensions of the surface cell (which is then periodically repeated in two dimensions) needs to be made.[42] In the present case, it turned out that the most stable structures for

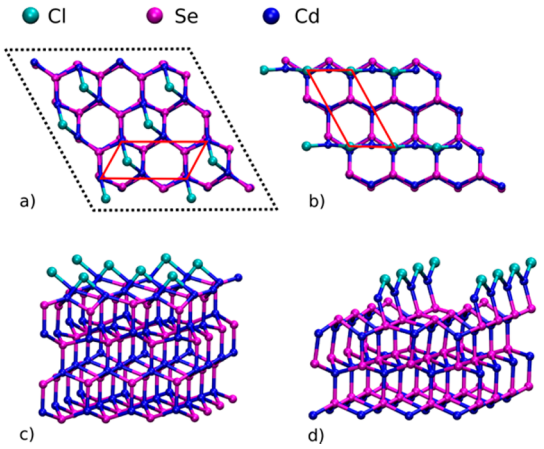

Figure 4. Models of the Cl-complexed (a,c) CdSe(0001) and (b,d) CdSe bulk surfaces. (a,b) Top view and (c,d) tilted view of the DFT-optimized geometries. The primitive surface unit cell is represented by red lines in (a,b). For comparison, the surface unit cell employed in the simulation is shown for CdSe(0001) using dashed black lines (a). For the sake of clarity, in (c,d) only the first three subsurface CdSe layers are shown.

the two polar facets are those reported in Figure 4 (see also SI). A common feature of these structures is that Cl atoms tend to bridge Cd atoms on the surface. However, for the (0001) termination, with the Cd dangling bonds pointing upward and perpendicular to the surface, a Cl atom bridging two Cd atoms involves a serious distortion of the bonds (Figure 4a and 4c).

For the bulk CdSe(000$\bar{1}$) surface, fulfillment of electron counting rules required the removal of half of the surface Cd atoms (Figure 4b and 4d). The remaining Cd atoms, with their three dangling bonds, each forming an angle of 60° with the surface normal, could easily be bridged by Cl atoms, with little bond distortion. This configuration leaves one dangling bond empty per surface Cd atom, which could ideally be saturated by other electron donating molecules (like the alkylphosphonate moieties that were found by our analyses to share surface passivation with the Cl^- ions). We also computed the removal energy of one Cl atom from both surfaces, in order to estimate the affinity of Cl for the two terminations. In line with the experimental Cl-induced stabilization of the (000$\bar{1}$) facet, the desorption energy of Cl from the CdSe(000$\bar{1}$) surface is 0.67 eV larger than from the CdSe(0001) one.

An important issue in calculations of the type reported here is that, since polar surfaces tend to reconstruct, a supercell must be large enough to allow for such reconstruction to be correctly modeled. We have taken care of size effects by employing a surface supercell as large as 4 × 4 bulk terminations. Reconstruction was modeled by letting the surfaces comply with the electron counting rule. After relaxation, the reconstructed surfaces displayed a 2 × 1 primitive surface unit cell, which could be well represented within the 4 × 4 supercell employed for the calculations.

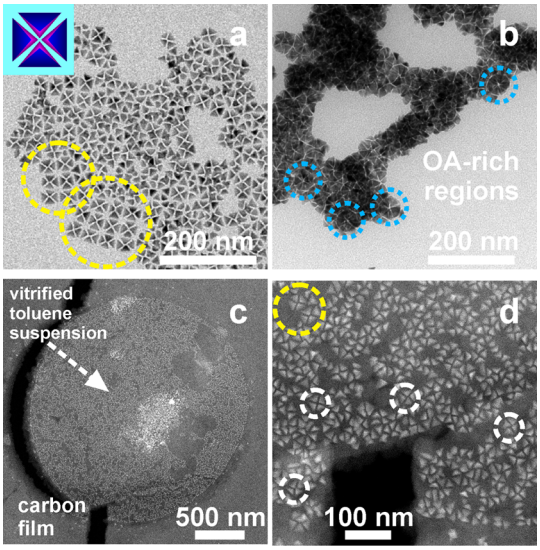

Figure 5. Self-assembly experiments on CdSe NPYs. (a,b) BFTEM images of typical NPY patterns observed after the second addition of oleic acid (OA) to the NPY suspension in toluene: after OA addition, (a) remarkable patterns of clovers are observed in some regions, extended up to 200 nm (within yellow circles), while (b) more complex, flower-like shapes appear in OA-rich regions (within cyan circles). (c,d) HAADF-STEM images of a vitrified suspension of NPYs in toluene after OA addition: in (c) a circular hole in the Quantifoil holey film, clearly filled with the vitrified suspension and broken at one edge, is visible. In (d) some isolated NPY clovers (white circles) are visible within the hole, while only few neighboring ones are found (yellow circle).

The surface supercell is reported in Figure 4a (in black dashed lines). As a further check, we also replicated the optimized $(000\bar{1})$ structure along the surface directions, to obtain an 8×8 surface supercell model. DFT geometry optimization on the 8×8 surface was carried out using the same convergence thresholds employed for the other calculations, and yielded basically no change in the structural features with respect to the 4×4 surface model.

Although we have no direct experimental tool sensitive enough to verify that the NPY lateral facets are differently passivated compared to the basal facet, which is expected due to their differential polarity, we obtained indirect indications in that regard from NPY assembly experiments. When OA was added to the size-selected NPYs, they assembled into "clovers", consisting of four NPYs with their nonpolar lateral facets congregating toward the center and the polar basal planes pointing outward, as shown in Figure 5a. Within the clovers, the lateral NPY facets are roughly parallel to each other, at an average distance of 3.2($\pm$0.6) nm. In OA-rich areas, more complex, flower-like shapes were formed, as shown in Figure 5b. Short range ordering of few clovers was additionally observed, with the NPY bases roughly facing each other, with an edge-to-edge distance of about 3 nm, and an angle of about 120° between adjacent basal facets of the interacting NPYs (within yellow circles in Figure 5a). To the best of our knowledge, such a clover assembly of NPYs has never been reported, while for similar shapes tail-to-tail structures are more often reported.[43]

An unequivocal proof that the clover patterns were formed in solution, and not upon solvent evaporation, came from cryo-TEM investigation of a suitably prepared suspension of NPYs in its vitrified form. In Figure 5c, a circular hole is shown in the carbon support film, filled with a meniscus of vitrified toluene containing NPYs. Several clover assemblies are found within the meniscus (Figure 5d, white circles), while only few side-to-side clovers are observed (yellow circle). This might be explained by a slight disturbance of the local order upon the preparation of the cryo-TEM sample.

Interestingly, the fact that crystallographically equivalent facets (the $\{40\bar{4}5\}$ ones) come together in the formation of clovers suggests that they have similar ligand shell characteristics/density, which should be different from that of the basal facets (the $(000\bar{1})$ facets), as these are not involved in the nearly parallel face-to-face assembly. Since carboxylic acids tend to "self-associate" through hydrogen bonds between the carboxyl groups (thereby forming dimers in a nonpolar solvent), we assume that these dimers are at play here giving rise to the clovers. Similar long chain (C_{12}–C_{18}) thiols or amines had no effect on the size-selection or clover-formation, which bears further strength to the above argument since the intermolecular hydrogen-bonding is much weaker in these molecules. The separation between the NPYs is larger than the diameter of the OA molecules which means that the depletion attraction forces are not operative here.[44] We also did not observe any kind of ordering on slow diffusion of the antisolvent to a toluene solution of the NPYs.

These observations can be rationalized if we assume that the OA dimers stabilize the clovers by interdigitating, through their two alkyl chains pointing outward, with the alkyl chains of the phosphonate molecules bound to the surface Cd-atoms, *via* hydrophobic interactions. This observation is further corroborated by the fact that these clovers cease to exist when they are washed with a toluene/methanol mixture. However, the clovers (Figure 5a) are not as close-packed as one would assume since the overcrowding of polar [0001] tips of the different NPYs most likely makes the congregation energetically unfavorable due to the electrostatic repulsion among the tip-dipoles. We hypothesize that OA strikes a balance between the electrostatic repulsion and the hydrophobic interaction (between the phosphonate and oleate carbon backbones) resulting in the observed short-range order.

As a final experiment, the effect of the unusual polarity of these CdSe NPYs was tested by employing them as seeds for the growth of wurtzite CdS pods, carried out in conditions favoring the development of ⟨0001⟩ elongated pods (see Methods section for details on the synthesis).[28] The wurtzite structure of the CdS

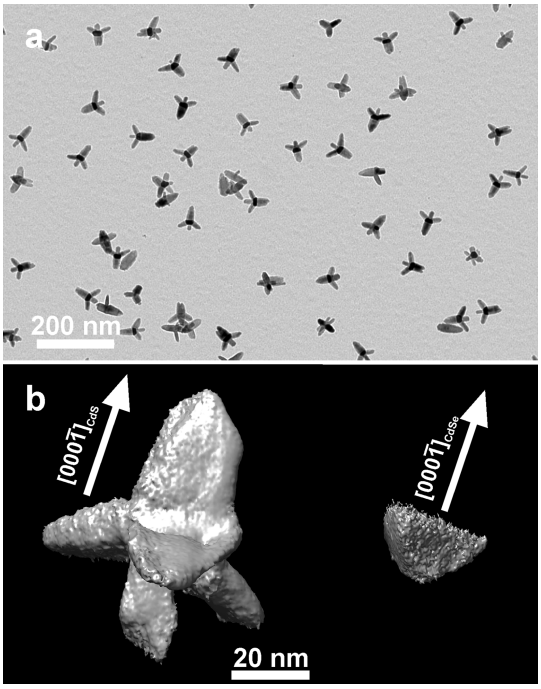

Figure 6. Seeded growth of CdS pods on the CdSe NPYs. (a) Overview BFTEM image of the branched CdSe(seeds)/CdS (pods) NCs. (b) Iso-surface view of reconstructed volume (*via* HAADF-STEM tomography) of a branched CdSe(core)/CdS-(pods) NC showing the presumed crystallographic growth direction of the CdS pod. On the right in (b), the volume reconstruction of a NPY in the orientation proposed as the initial seed orientation relative to the final rocket shape.

pods was elucidated by XRD analyses (Figure S7). The resulting branched-NCs exhibit a peculiar rocket-like shape, dominated by a central asymmetrical pod, with a sharper tip in the longer part and a flatter end in its opposite section, and three shorter pods in the direction of the short axial pod (Figure 6a). The 3D shape of these rocket NCs was clarified by electron tomography-based volume reconstruction (Figure 6b), clearly showing the major axial pod, with different endings, and three axially symmetrical branches departing from it, at a position closer to the shorter flat end (presumably, the position of the initial CdSe seed). In addition to this, each of these lateral pods forms a ~60° angle with respect to the central axis, in significant agreement with the orientation of NPY lateral facets. On the basis of former results obtained using similar conditions for CdS seeded growth,[35] we are rather confident that the tip of the axial pod points toward the [000$\bar{1}$] direction of CdS. As in the employed synthesis conditions CdS pods grow epitaxially on the CdSe seeds, also taking the polarity information from them, and the lateral pods show the same orientation as the lateral facets of the initial CdSe NPYs, we can estimate how the five pods in these unusual rocket NCs developed: the four tetrahedrally arranged pods, exhibiting sharper tips, result from CdS nucleation on the four NPY facets, and in particular the NPY base ((000$\bar{1}$) facet) acts as nucleation facet for the longer axial pod, ending with a rather sharp tip. Instead, the shorter axial pod, showing a flat end, develops from the NPY tip. Elemental mapping by STEM-EDS did not show a clear shape of the CdSe core within the multipod (Figure S8), either due to its small size compared to the multipod NC or to its partial etching upon seeded growth conditions; hence, it was not possible to directly prove this statement.

CONCLUSIONS

We have demonstrated that the introduction of Cl^- ions into the typical synthesis environment for wurtzite CdSe NCs leads to the formation of rather monodisperse pyramidal-shaped CdSe NCs, by imparting higher thermodynamic stability to the polar (000$\bar{1}$) facet which serves as the NPY base, while the (0001) facet is essentially reduced to the pyramid apex. The observed crystal polarity exhibited by these CdSe NPYs is in contrast to earlier studies where the opposite scenario was demonstrated for colloidal synthesis of Cd chalcogenide NCs, performed without the deliberate addition of Cl^- ions. Our experimental observations, based on advanced TEM techniques, were corroborated by DFT calculations on possible binding configurations of Cl atoms on the (0001) and (000$\bar{1}$) facets. The characteristically different facets of the NPYs, *i.e.*, one basal and the three equivalent lateral facets, should also differ in ligand density and makeup, since oleic acid-driven self-assembly experiments reveal that the NPYs interact with each other almost exclusively through their lateral facets and much more weakly through their basal facets, leading to the formation of isolated "clover-like" units. Finally, peculiar multipod NCs were synthesized when the CdSe NPYs were used as seeds for wurtzite CdS pods growth: we could show, based on simple geometrical arguments, that the morphology of the branched structures corroborates the reversed polarity of the CdSe seeds. This approach, if confirmed by tailored experiments, would indicate that the seeded growth of wurtzite CdS branches is a rather cost- and time-effective way to test the polarity of Cd chalcogenide NCs.

METHODS

Materials. Cadmium oxide (CdO, 99.999%), cadmium chloride ($CdCl_2$, 99.99%) and oleic acid (OA, 90%) were purchased from Sigma-Aldrich. Tri-*n*-octylphosphine oxide (TOPO, 99%), tri-*n*-octylphosphine (TOP, 97%), and selenium powder (Se, 99.99%) were procured from Strem Chemicals. *N*-Octadecylphosphonic acid (ODPA) and *n*-hexylphosphonic acid (HPA) were obtained from Polycarbon Industries. Anhydrous methanol and toluene were purchased from Carlo Erba reagents. All chemicals were used as received.

Synthesis of CdSe NPYs. All the synthetic endeavors were undertaken through a standard Schlenk line technique aided

by a nitrogen filled glovebox. CdO (100 mg; 0.78 mmol), $CdCl_2$ (36 mg; 0.2 mmol), HPA (42 mg; 0.25 mmol), ODPA (42 mg; 0.13 mmol) and TOPO (3 g; 7.75 mmol) were mixed in a 25 mL round-bottomed flask and degassed under vacuum at a temperature of 120 °C for 1 h. The flask was then backfilled with nitrogen and the temperature was raised to 350 °C. At this temperature the mixture was in the form of pale yellow suspension (*i.e.*, it was not optically clear), indicating a not complete dissolution of $CdO/CdCl_2$. This is expected, as the actual molar ratio of phosphonic acids present (HPA+ODPA) to cadmium ($CdO+CdCl_2$) was only ~0.4:1, that is, much lower than 2:1, which was found in previous works as the lower limit for complete complexation of the Cd ions. This was also confirmed by XRD analysis of the complex, after precipitation and washing with methanol, which exhibited a pattern mainly ascribable to CdO.

The reaction mixture was stirred at this temperature for 10 min to complete the Cd-phosphonate complexation. At this point, Se:TOP (0.5 mL; prepared at a concentration of 72 mg of Se per mL of TOP in a nitrogen filled glovebox) solution was injected swiftly into the flask which resulted in a dark-brown solution almost instantaneously, indicating the formation of the tetrahedral CdSe NPYs. The reaction was allowed to run for 5 min and the heating mantle was removed afterward to let the solution cool down. The final brown solution was then suspended in toluene and washed with methanol. The NPYs were resuspended in toluene and further centrifuged at 1000−2000 rpm for a couple of minutes to remove larger particles formed during the reaction. Aliquots of the reaction mixture were drawn out at several time intervals to monitor the growth process.

Size Selection and Self-Assembly Experiments. The NPY-synthesis produces some branched structures as well (*e.g.*, tetrapods, tripods, irregular structures *etc.*), which were removed by washing with OA. OA selectively flocculates the NPYs, which were precipitated by centrifugation. The supernatant was discarded and the size-selected NPYs were redispersed in toluene. Further addition of OA into a toluene solution of size-selected NPYs led to the observation of the clovers with short-range ordering.

Seeded Growth of CdS Pods on the CdSe NPYs. CdO (60 mg; 0.47 mmol), $CdCl_2$ (6 mg; 0.033 mmol), HPA (80 mg; 0.48 mmol), ODPA (290 mg; 0.87 mmol) and TOPO (3 g; 7.75 mmol) were loaded in a 25 mL round-bottomed flask and degassed under vacuum at a temperature of 120 °C for 1 h. Subsequently, the flask was backfilled with nitrogen and the temperature was raised to 380 °C, which led to the formation of transparent Cd-phosphonate complex from the earlier red suspension. Two mL of TOP was injected at this point leading to a sharp dip in the temperature which were allowed to recover to 380 °C. An injection solution comprising of a mixture of CdSe NPYs (100 μL, 2.5 μM in TOP) and S:TOP (0.5 g; prepared at a concentration of 90 mg of S per mL of TOP), mixed in a nitrogen filled glovebox, was then swiftly introduced in the reaction mixture. The transparent solution turned dark brown in a course of few minutes which was left to stir for 30 min. The heating mantle was removed at the end of the reaction and the solution was allowed to cool down. Toluene was added to this mixture and the branched nanostructures were washed twice with methanol. The nanostructures were redispered in toluene.

Transmission Electron Microscopy (TEM) Analysis. BFTEM images and SAED patterns were acquired on samples prepared by drop-casting a concentrated solution of NCs on carbon-coated 200 mesh copper grids, using a JEOL JEM-1011 microscope (W filament) operated at a 100 kV accelerating voltage. HRTEM, HAADF−STEM and EDS analyses were performed with a JEOL JEM-2200FS microscope equipped with a Schottky emitter operated at 200 kV, a CEOS image corrector allowing for an information limit of 0.8 Å, and an in-column energy filter (Ω-type). For EW reconstruction, a series of 20 images at different foci was acquired (−30 μm spherical aberration, 8 nm nominal focus step). The EW was extracted by back-projecting the images using the IWFR software (HREM Research Inc.). The chemical compositions of the NCs were determined by EDS, performed in HAADF-STEM mode, using a Bruker Quantax 400 system with a 60 mm^2 XFlash 6T silicon drift detector (SDD). Aberration-corrected HAADF-STEM images were acquired using a probe-corrected Titan "cubed" microscope operated at 200 kV, with a 0.08 nm probe (22 mrad convergence, 38 mrad inner ADF angle). The contrast in the HAADF images was simulated using the linear model approximation proposed by Kirkland[45] and implemented in STEM_CELL.[46] For high resolution imaging the NC suspensions were drop-cast on copper grids covered with a holey amorphous carbon film. For STEM-EDS analyses the NC suspensions were deposited onto carbon-coated 150 mesh Cu grids for and the measurements were carried out using a holder with a beryllium cup for background reduction.

Cryo-TEM experiments were carried out in HAADF-STEM mode on a FEI Tecnai G2 F20 TWIN instrument, equipped with a Schottky emitter operated at 200 kV and using a Gatan cryo-transfer holder (Mod. 914). For these analyses, the samples were prepared by vitrifying suitably prepared NC suspensions in toluene deposited onto Quantifoil holey carbon films on Cu grids by means of the FEI Vitrobot.

For the acquisition of the tilt series for tomography, few μL of the NC suspensions were deposited onto carbon-coated 150 mesh Cu grids. The HAADF-STEM tilted images series were acquired by the aforementioned Tecnai F20 TEM over an angular range of −70° to +70° with a 2° step. Alignment based on cross-correlation and sample tomograms (without fiducial markers) was applied to the tilt series using IMOD.[47] The volume reconstruction was then performed *via* 20 simultaneous iterative reconstruction technique (SIRT) iterations using IMOD. The reported surface rendering was performed using the UCSF Chimera package.[48]

X-ray Diffraction (XRD) Analysis. Concentrated solution of the NC samples were drop-cast (followed by evaporation of the solvent) on a zero background silicon substrate for acquiring the XRD patterns which was performed on a Rigaku SmartLab 9 kW diffractometer with the X-ray source operating at 40 kV and 150 mA. The instrument was equipped with a Cu source and a Göbel mirror (to obtain a parallel beam and suppress the Cu Kβ radiation at 1.392 Å) and was used in the $2\theta/\omega$ scan geometry for data acquisition. Phase identification was performed through the assistance of PDXL software

Computational Details. Calculations have been performed using the CP2K code.[49] We used double-ζ valence basis sets with one polarization function (DZVP) for all elements,[50] Perdew−Burke−Enzerhof (PBE) functional[51] and Goedecker−Teter−Hutter (GTH) pseudopotentials.[52] Geometry optimization of the system was performed until the largest force on atoms was below 0.002 Hartree/Bohr. The charge density of the system was expanded in plane waves for the calculation of the Poisson equation during the self-consistent field cycle, employing a cutoff of 400 Ry. The bulk lattice parameters of the CdSe wurtzite were optimized by isotropic cell relaxation, and the lowest energy structure corresponded to an expansion of 2.6% with respect to the experimental result. Such an overestimation of the lattice parameter of solids is expected for the PBE functional.[53] We used slabs including 8 layers of CdSe along the [0001] direction and a surface encompassing 4×4 bulk termination unit cells. For bare CdSe (0001) and (000$\bar{1}$) surfaces, this results in slabs including 256 atoms. The periodic slab calculations included a vacuum layer of 20 Å, which separates the surfaces in the periodic image representation of the system. The two bottom layers of the slab were kept fixed to bulk-like position.

To rule out possible dependencies on the basis set chosen, we also run test calculations using the plane wave code Quantum Espresso.[54] Ultrasoft pseudopotentials were used for all elements.[55] The plane wave and charge density cutoff were set to 40 and 320 Ry, respectively. The PBE functional was used. The optimal lattice parameter corresponded to an expansion of 1.3% with respect to the experimental result. Bare bulk Cd terminated surfaces of (000$\bar{1}$) CdSe were simulated using the same initial geometry employed for the CP2K calculations, with the only exception of a reduced number of layers (6 instead of 8) included in the direction perpendicular to the surface. Bader charges and bond orders in the systems were computed using the approaches described in the literature.[56−58]

Conflict of Interest: The authors declare no competing financial interest.

Acknowledgment. The authors gratefully acknowledge L. Maserati and M. Arciniegas for stimulating discussions. The research leading to these results has received funding from the European Commission FP7 under the ERC Consolidator Grant "TRANS-NANO" (grant agreement no. 614897) and the Integrated Infrastructure Initiative ESTEEM2 (grant agreement no. 312483). S.T. gratefully acknowledges the FWO Flanders for a postdoctoral scholarship.

Supporting Information Available: Description of additional experiments and details on the theoretical calculations. Ligand exchange experiments on the NPYs (in comparison to CdSe nanorods synthesized without the deliberate addition of chloride ions) monitored through XPS and NMR spectroscopy. TEM, XRD, optical properties and STEM-EDS analyses on CdSe NPYs and nanorods and on CdSe/CdS branched NCs. The Supporting Information is available free of charge on the ACS Publications website at DOI: 10.1021/acsnano.5b03636.

REFERENCES AND NOTES

1. Gur, I.; Fromer, N. A.; Geier, M. L.; Alivisatos, A. P. Air-Stable All-Inorganic Nanocrystal Solar Cells Processed from Solution. *Science* **2005**, *310*, 462–465.
2. Kim, J. Y.; Voznyy, O.; Zhitomirsky, D.; Sargent, E. H. 25th Anniversary Article: Colloidal Quantum Dot Materials and Devices: A Quarter-Century of Advances. *Adv. Mater.* **2013**, *25*, 4986–5010.
3. Zhao, M.-X.; Li, Y.; Zeng, E.-Z.; Wang, C.-J. The Application of CdSe Quantum Dots with Multicolor Emission as Fluorescent Probes for Cell Labeling. *Chem. - Asian J.* **2014**, *9*, 1349–1355.
4. Dimitrijevic, J.; Krapf, L.; Wolter, C.; Schmidtke, C.; Merkl, J.-P.; Jochum, T.; Kornowski, A.; Schüth, A.; Gebert, A.; Hüttmann, G.; *et al.* CdSe/CdS-Quantum Rods: Fluorescent Probes for *in vivo* Two-Photon Laser Scanning Microscopy. *Nanoscale* **2014**, *6*, 10413–10422.
5. Anikeeva, P. O.; Halpert, J. E.; Bawendi, M. G.; Bulović, V. Quantum Dot Light-Emitting Devices with Electroluminescence Tunable over the Entire Visible Spectrum. *Nano Lett.* **2009**, *9*, 2532–2536.
6. Yin, Y.; Alivisatos, A. P. Colloidal Nanocrystal Synthesis and the Organic–Inorganic Interface. *Nature* **2005**, *437*, 664–670.
7. Murray, C. B.; Norris, D. J.; Bawendi, M. G. Synthesis and Characterization of Nearly Monodisperse CdE (E = Sulfur, Selenium, Tellurium) Semiconductor Nanocrystallites. *J. Am. Chem. Soc.* **1993**, *115*, 8706–8715.
8. Murray, C. B.; Sun, S.; Gaschler, W.; Doyle, H.; Betley, T. A.; Kagan, C. R. Colloidal Synthesis of Nanocrystals and Nanocrystal Superlattices. *IBM J. Res. Dev.* **2001**, *45*, 47–56.
9. Deka, S.; Genovese, A.; Zhang, Y.; Miszta, K.; Bertoni, G.; Krahne, R.; Giannini, C.; Manna, L. Phosphine-Free Synthesis of p-Type Copper(I) Selenide Nanocrystals in Hot Coordinating Solvents. *J. Am. Chem. Soc.* **2010**, *132*, 8912–8914.
10. Mulvihill, M. J.; Habas, S. E.; Plante, I. J.-L.; Wan, J.; Mokari, T. Influence of Size, Shape, and Surface Coating on the Stability of Aqueous Suspensions of CdSe Nanoparticles. *Chem. Mater.* **2010**, *22*, 5251–5257.
11. De Trizio, L.; Figuerola, A.; Manna, L.; Genovese, A.; George, C.; Brescia, R.; Saghi, Z.; Simonutti, R.; Van Huis, M.; Falqui, A. Size-Tunable, Hexagonal Plate-like Cu_3P and Janus-like Cu–Cu_3P Nanocrystals. *ACS Nano* **2011**, *6*, 32–41.
12. Miao, S.; Hickey, S. G.; Rellinghaus, B.; Waurisch, C.; Eychmüller, A. Synthesis and Characterization of Cadmium Phosphide Quantum Dots Emitting in the Visible Red to Near-Infrared. *J. Am. Chem. Soc.* **2010**, *132*, 5613–5615.
13. Xie, R.; Battaglia, D.; Peng, X. Colloidal InP Nanocrystals as Efficient Emitters Covering Blue to Near-Infrared. *J. Am. Chem. Soc.* **2007**, *129*, 15432–15433.
14. Chan, E. M.; Xu, C.; Mao, A. W.; Han, G.; Owen, J. S.; Cohen, B. E.; Milliron, D. J. Reproducible, High-Throughput Synthesis of Colloidal Nanocrystals for Optimization in Multidimensional Parameter Space. *Nano Lett.* **2010**, *10*, 1874–1885.
15. Wang, F.; Tang, R.; Buhro, W. E. The Trouble with TOPO; Identification of Adventitious Impurities Beneficial to the Growth of Cadmium Selenide Quantum Dots, Rods, and Wires. *Nano Lett.* **2008**, *8*, 3521–3524.
16. Wang, F.; Tang, R.; Kao, J. L.-F.; Dingman, S. D.; Buhro, W. E. Spectroscopic Identification of Tri-*n*-octylphosphine Oxide (TOPO) Impurities and Elucidation of Their Roles in Cadmium Selenide Quantum-Wire Growth. *J. Am. Chem. Soc.* **2009**, *131*, 4983–4994.
17. Wolcott, A.; Fitzmorris, R. C.; Muzaffery, O.; Zhang, J. Z. CdSe Quantum Rod Formation Aided By *In Situ* TOPO Oxidation. *Chem. Mater.* **2010**, *22*, 2814–2821.
18. Steckel, J. S.; Yen, B. K. H.; Oertel, D. C.; Bawendi, M. G. On the Mechanism of Lead Chalcogenide Nanocrystal Formation. *J. Am. Chem. Soc.* **2006**, *128*, 13032–13033.
19. Houtepen, A. J.; Koole, R.; Vanmaekelbergh, D.; Meeldijk, J.; Hickey, S. G. The Hidden Role of Acetate in the PbSe Nanocrystal Synthesis. *J. Am. Chem. Soc.* **2006**, *128*, 6792–6793.
20. Bae, W. K.; Joo, J.; Padilha, L. A.; Won, J.; Lee, D. C.; Lin, Q.; Koh, W.-k.; Luo, H.; Klimov, V. I.; Pietryga, J. M. Highly Effective Surface Passivation of PbSe Quantum Dots through Reaction with Molecular Chlorine. *J. Am. Chem. Soc.* **2012**, *134*, 20160–20168.
21. Zhang, J.; Gao, J.; Miller, E. M.; Luther, J. M.; Beard, M. C. Diffusion-Controlled Synthesis of PbS and PbSe Quantum Dots with *in Situ* Halide Passivation for Quantum Dot Solar Cells. *ACS Nano* **2013**, *8*, 614–622.
22. Ning, Z.; Voznyy, O.; Pan, J.; Hoogland, S.; Adinolfi, V.; Xu, J.; Li, M.; Kirmani, A. R.; Sun, J.-P.; Minor, J.; *et al.* Air-Stable n-Type Colloidal Quantum Dot Solids. *Nat. Mater.* **2014**, *13*, 822–828.
23. Tang, J.; Kemp, K. W.; Hoogland, S.; Jeong, K. S.; Liu, H.; Levina, L.; Furukawa, M.; Wang, X.; Debnath, R.; Cha, D.; *et al.* Colloidal-Quantum-Dot Photovoltaics Using Atomic-Ligand Passivation. *Nat. Mater.* **2011**, *10*, 765–771.
24. Wu, W.-Y.; Chakrabortty, S.; Chang, C. K. L.; Guchhait, A.; Lin, M.; Chan, Y. Promoting 2D Growth in Colloidal Transition Metal Sulfide Semiconductor Nanostructures *via* Halide Ions. *Chem. Mater.* **2014**, *26*, 6120–6126.
25. Lohse, S. E.; Burrows, N. D.; Scarabelli, L.; Liz-Marzán, L. M.; Murphy, C. J. Anisotropic Noble Metal Nanocrystal Growth: The Role of Halides. *Chem. Mater.* **2013**, *26*, 34–43.
26. Scarabelli, L.; Coronado-Puchau, M.; Giner-Casares, J. J.; Langer, J.; Liz-Marzán, L. M. Monodisperse Gold Nanotriangles: Size Control, Large-Scale Self-Assembly, and Performance in Surface-Enhanced Raman Scattering. *ACS Nano* **2014**, *8*, 5833–5842.
27. Gómez-Graña, S.; Goris, B.; Altantzis, T.; Fernández-López, C.; Carbó-Argibay, E.; Guerrero-Martínez, A.; Almora-Barrios, N.; López, N.; Pastoriza-Santos, I.; Pérez-Juste, J.; *et al.* Au@Ag Nanoparticles: Halides Stabilize {100} Facets. *J. Phys. Chem. Lett.* **2013**, *4*, 2209–2216.
28. Kim, M. R.; Miszta, K.; Povia, M.; Brescia, R.; Christodoulou, S.; Prato, M.; Marras, S.; Manna, L. Influence of Chloride Ions on the Synthesis of Colloidal Branched CdSe/CdS Nanocrystals by Seeded Growth. *ACS Nano* **2012**, *6*, 11088–11096.
29. Saruyama, M.; Kanehara, M.; Teranishi, T. Drastic Structural Transformation of Cadmium Chalcogenide Nanoparticles Using Chloride Ions and Surfactants. *J. Am. Chem. Soc.* **2010**, *132*, 3280–3282.
30. Lim, S. J.; Kim, W.; Jung, S.; Seo, J.; Shin, S. K. Anisotropic Etching of Semiconductor Nanocrystals. *Chem. Mater.* **2011**, *23*, 5029–5036.
31. Meyns, M.; Iacono, F.; Palencia, C.; Geweke, J.; Coderch, M. D.; Fittschen, U. E. A.; Gallego, J. M.; Otero, R.; Juárez, B. H.; Klinke, C. Shape Evolution of CdSe Nanoparticles Controlled by Halogen Compounds. *Chem. Mater.* **2014**, *26*, 1813–1821.
32. Miszta, K.; Brescia, R.; Prato, M.; Bertoni, G.; Marras, S.; Xie, Y.; Ghosh, S.; Kim, M. R.; Manna, L. Hollow and Concave Nanoparticles *via* Preferential Oxidation of the Core in Colloidal Core/Shell Nanocrystals. *J. Am. Chem. Soc.* **2014**, *136*, 9061–9069.

33. Christodoulou, S.; Rajadell, F.; Casu, A.; Vaccaro, G.; Grim, J. Q.; Genovese, A.; Manna, L.; Climente, J. I.; Meinardi, F.; Rainò, G.; *et al.* Band Structure Engineering *via* Piezoelectric Fields in Strained Anisotropic CdSe/CdS Nanocrystals. *Nat. Commun.* **2015**, *6*, 7905.
34. Palencia, C.; Lauwaet, K.; de la Cueva, L.; Acebrón, M.; Conde, J. J.; Meyns, M.; Klinke, C.; Gallego, J. M.; Otero, R.; Juárez, B. H. Cl-capped CdSe nanocrystals *via in situ* generation of chloride anions. *Nanoscale* **2014**, *6*, 6812–6818.
35. Bertoni, G.; Grillo, V.; Brescia, R.; Ke, X.; Bals, S.; Catellani, A.; Li, H.; Manna, L. Direct Determination of Polarity, Faceting, and Core Location in Colloidal Core/Shell Wurtzite Semiconductor Nanocrystals. *ACS Nano* **2012**, *6*, 6453–6461.
36. Li, Y.; Mastria, R.; Fiore, A.; Nobile, C.; Yin, L.; Biasiucci, M.; Cheng, G.; Cucolo, A. M.; Cingolani, R.; Manna, L.; *et al.* Improved Photovoltaic Performance of Heterostructured Tetrapod-Shaped CdSe/CdTe Nanocrystals Using C60 Interlayer. *Adv. Mater.* **2009**, *21*, 4461–4466.
37. Choi, C. L.; Koski, K. J.; Olson, A. C. K.; Alivisatos, A. P. Luminescent nanocrystal stress gauge. *Proc. Natl. Acad. Sci. U. S. A.* **2010**, *107*, 21306–21310.
38. Urban, K. W.; Jia, C.-L.; Houben, L.; Lentzen, M.; Mi, S.-B.; Tillmann, K. Negative Spherical Aberration Ultrahigh-Resolution Imaging in Corrected Transmission Electron Microscopy. *Philos. Trans. R. Soc., A* **2009**, *367*, 3735–3753.
39. Hungría, A. B.; Juárez, B. H.; Klinke, C.; Weller, H.; Midgley, P. A. 3-D Characterization of CdSe Nanoparticles Attached to Carbon Nanotubes. *Nano Res.* **2008**, *1*, 89–97.
40. Gomes, R.; Hassinen, A.; Szczygiel, A.; Zhao, Q.; Vantomme, A.; Martins, J. C.; Hens, Z. Binding of Phosphonic Acids to CdSe Quantum Dots: A Solution NMR Study. *J. Phys. Chem. Lett.* **2011**, *2*, 145–152.
41. Iacono, F.; Palencia, C.; de la Cueva, L.; Meyns, M.; Terracciano, L.; Vollmer, A.; de la Mata, M. J.; Klinke, C.; Gallego, J. M.; Juarez, B. H.; *et al.* Interfacing Quantum Dots and Graphitic Surfaces with Chlorine Atomic Ligands. *ACS Nano* **2013**, *7*, 2559–2565.
42. Manna, L.; Wang, L.; Cingolani, R.; Alivisatos, A. P. First-Principles Modeling of Unpassivated and Surfactant-Passivated Bulk Facets of Wurtzite CdSe: A Model System for Studying the Anisotropic Growth of CdSe Nanocrystals. *J. Phys. Chem. B* **2005**, *109*, 6183–6192.
43. Javon, E.; Gaceur, M.; Dachraoui, W.; Margeat, O.; Ackermann, J.; Saba, M. I.; Delugas, P.; Mattoni, A.; Bals, S.; Van Tendeloo, G. Competing Forces in the Self-Assembly of Coupled ZnO Nanopyramids. *ACS Nano* **2015**, *9*, 3685–3694.
44. Baranov, D.; Fiore, A.; van Huis, M.; Giannini, C.; Falqui, A.; Lafont, U.; Zandbergen, H.; Zanella, M.; Cingolani, R.; Manna, L. Assembly of Colloidal Semiconductor Nanorods in Solution by Depletion Attraction. *Nano Lett.* **2010**, *10*, 743–749.
45. Kirkland, E. J. *Advanced Computing in Electron Microscopy*; Plenum Press: New York, 1998.
46. Grillo, V.; Rotunno, E. STEM_CELL: A Software Tool for Electron Microscopy: Part I - Simulations. *Ultramicroscopy* **2013**, *125*, 97–111.
47. Kremer, J. R.; Mastronarde, D. N.; McIntosh, J. R. Computer Visualization of Three-Dimensional Image Data Using IMOD. *J. Struct. Biol.* **1996**, *116*, 71–76.
48. Pettersen, E. F.; Goddard, T. D.; Huang, C. C.; Couch, G. S.; Greenblatt, D. M.; Meng, E. C.; Ferrin, T. E. UCSF Chimera—A Visualization System for Exploratory Research and Analysis. *J. Comput. Chem.* **2004**, *25*, 1605–1612.
49. Hutter, J.; Iannuzzi, M.; Schiffmann, F.; VandeVondele, J. cp2k: Atomistic Simulations of Condensed Matter Systems. *WIREs Comput. Mol. Sci.* **2014**, *4*, 15–25.
50. VandeVondele, J.; Hutter, J. Gaussian Basis Sets for Accurate Calculations on Molecular Systems in Gas and Condensed Phases. *J. Chem. Phys.* **2007**, *127*, 114105.
51. Perdew, J. P.; Burke, K.; Ernzerhof, M. Generalized Gradient Approximation Made Simple. *Phys. Rev. Lett.* **1996**, *77*, 3865–3868.
52. Goedecker, S.; Teter, M.; Hutter, J. Separable dual-space Gaussian pseudopotentials. *Phys. Rev. B: Condens. Matter Mater. Phys.* **1996**, *54*, 1703–1710.
53. Csonka, G. I.; Perdew, J. P.; Ruzsinszky, A.; Philipsen, P. H. T.; Lebègue, S.; Paier, J.; Vydrov, O. A.; Ángyán, J. G. Assessing the Performance of Recent Density Functionals for Bulk Solids. *Phys. Rev. B: Condens. Matter Mater. Phys.* **2009**, *79*, 155107.
54. Giannozzi, P.; Baroni, S.; Bonini, N.; Calandra, M.; Car, R.; Cavazzoni, C.; Ceresoli, D.; Chiarotti, G. L.; Cococcioni, M.; Dabo, I.; *et al.* QUANTUM ESPRESSO: a Modular and Open-Source Software Project for Quantum Simulations of Materials. *J. Phys.: Condens. Matter* **2009**, *21*, 395502.
55. Cd.pbe-dn-rrkjus_psl.0.2.UPF, Se.pbe-n-rrkjus_psl.0.2.UPF and Cl.pbe-n-rrkjus_psl.0.1.UPF from http://www.quantum-espresso.org (accessed 30th March 2015).
56. Angyan, J. G.; Loos, M.; Mayer, I. Covalent Bond Orders and Atomic Valence Indices in the Topological Theory of Atoms in Molecules. *J. Phys. Chem.* **1994**, *98*, 5244–5248.
57. Bader, R. F. W. *Atoms in Molecules: A Quantum Theory*; Oxford University Press: New York, 1994.
58. Tang, W.; Sanville, E.; Henkelman, G. A Grid-based Bader Analysis Algorithm without Lattice Bias. *J. Phys.: Condens. Matter* **2009**, *21*, 084204.